The Astrophysical Journal, 803:85 (12pp), 2015 April 20 doi:10.1088/0004-637X/803/2/85

FIRST HIGH-RESOLUTION SPECTROSCOPIC OBSERVATIONS OF AN ERUPTING PROMINENCE WITHIN A CORONAL MASS EJECTION BY THE INTERFACE REGION IMAGING SPECTROGRAPH (IRIS)

Wei Liu[1,2], Bart De Pontieu[1,3], Jean-Claude Vial[4], Alan M. Title[1], Mats Carlsson[3], Han Uitenbroek[5], Takenori J. Okamoto[6], Thomas E. Berger[7], and Patrick Antolin[8]
[1] Lockheed Martin Solar and Astrophysics Laboratory, 3251 Hanover Street, Palo Alto, CA 94304, USA; weiliu@lmsal.com
[2] W. W. Hansen Experimental Physics Laboratory, Stanford University, Stanford, CA 94305, USA
[3] Institute of Theoretical Astrophysics, University of Oslo, P.O. Box 1029, Blindern, NO-0315, Oslo, Norway
[4] Institut d'Astrophysique Spatiale, Université Paris XI/CNRS, F-91405, Orsay Cedex, France
[5] National Solar Observatory, P.O. Box 62, Sunspot, NM 88349, USA
[6] Institute of Space and Astronautical Science, Japan Aerospace Exploration Agency, Yoshinodai, Sagamihara, 252-5210, Japan
[7] NOAA Space Weather Prediction Center, Boulder, CO 80305, USA
[8] National Astronomical Observatory of Japan, 2-21-1 Osawa, Mitaka, Tokyo 181-8588, Japan
Received 2014 November 20; accepted 2015 February 15; published 2015 April 21

ABSTRACT

Spectroscopic observations of prominence eruptions associated with coronal mass ejections (CMEs), although relatively rare, can provide valuable plasma and three-dimensional geometry diagnostics. We report the first observations by the *Interface Region Imaging Spectrograph* mission of a spectacular fast CME/prominence eruption associated with an equivalent X1.6 flare on 2014 May 9. The maximum plane-of-sky and Doppler velocities of the eruption are 1200 and 460 km s^{-1}, respectively. There are two eruption components separated by ~200 km s^{-1} in Doppler velocity: a primary, bright component and a secondary, faint component, suggesting a hollow, rather than solid, cone-shaped distribution of material. The eruption involves a left-handed helical structure undergoing counterclockwise (viewed top-down) unwinding motion. There is a temporal evolution from upward eruption to downward fallback with less-than-free-fall speeds and decreasing nonthermal line widths. We find a wide range of Mg II k/h line intensity ratios (less than ~2 expected for optically-thin thermal emission): the lowest ever reported median value of 1.17 found in the fallback material, a comparably high value of 1.63 in nearby coronal rain, and intermediate values of 1.53 and 1.41 in the two eruption components. The fallback material exhibits a strong ($>5\sigma$) linear correlation between the k/h ratio and the Doppler velocity as well as the line intensity. We demonstrate that Doppler dimming of scattered chromospheric emission by the erupted material can potentially explain such characteristics.

Key words: Sun: activity – Sun: corona – Sun: coronal mass ejections (CMEs) – Sun: filaments, prominences – Sun: UV radiation

Supporting material: animations

1. INTRODUCTION

As one of the major drivers of space-weather disturbances, coronal mass ejections (CMEs; see Chen 2011; Webb & Howard 2012, for recent reviews) are powerful eruptions of typically 10^{15}–10^{16} g masses from the Sun traveling at 100 – 2000 km s^{-1} and involving energies of 10^{30}–10^{32} erg. CMEs seen in white light often exhibit a classic three-part morphology (e.g., Hundhausen et al. 1984; Schwenn 1996) consisting of a bright leading front surrounding a dark cavity containing a bright core. The core is identified as an erupting prominence (e.g., Tandberg-Hanssen 1995; Martin 1998; Labrosse et al. 2010; Mackay et al. 2010; Parenti 2014), some cool ($T \sim 10^4$ K) and dense "chromospheric" plasma residing in the hot ($T \sim 10^6$ K) and tenuous corona prior to its eruption.

Prominence eruptions and CMEs in general are conventionally detected with *global imaging instruments*, which can constrain the morphology and plane-of-sky (POS) velocity among other observables. Such observations are obtained either monochromatically (e.g., in Hα, extreme-ultraviolet [EUV], or white light; St. Cyr et al. 2000) or in multiple passbands (e.g., with the Coronal Multichannel Polarimeter; Tian et al. 2013).

Spectroscopic observations of prominence eruptions or CMEs within restricted fields of view (FOVs) of slit spectrographs, although comparably rare, can provide valuable, complementing plasma diagnostics, e.g., density, temperature, and Doppler velocity. Such observations were obtained (i) in the outer corona (1.4–10 $R_\odot$) by the UltraViolet Coronagraph Spectrometer (UVCS; e.g., Ciaravella et al. 1997; Raymond et al. 2003) on board the *Solar and Heliospheric Observatory* (*SOHO*) and (ii) in the inner corona ($r \lesssim 1.5\ R_\odot$) by spectroheliographs on *Skylab* (e.g., Schmahl & Hildner 1977; Widing et al. 1986), the Ultraviolet Spectrometer and Polarimeter on the *Solar Maximum Mission* (*SMM*; e.g., Fontenla & Poland 1989), the Solar Ultraviolet Measurements of Emitted Radiation and Coronal Diagnostic Spectrometer on *SOHO* (e.g., Wiik et al. 1997), the EUV Imaging Spectrometer on *Hinode* (e.g., Harra et al. 2007; Jin et al. 2009; Tian et al. 2012; D. R. Williams et al. 2015, in preparation), and ground-based instruments (e.g., Penn 2000). Notably, during 1996–2005, UVCS detected >1000 CMEs (Giordano et al. 2013), about 10% of the CMEs detected by the *SOHO* Large Angle and Spectrometric Coronagraph (LASCO) during the same period. The most commonly detected feature of UVCS CMEs (in ~70% of them) is the cool prominence material.

The recently launched *Interface Region Imaging Spectrograph* mission (*IRIS*; De Pontieu et al. 2014), thanks to its advanced capabilities over previous generations of instruments, has provided a new opportunity to observe CMEs and

especially prominence eruptions in unprecedented detail. *IRIS* offers a high resolution of 0.″33–0.″4 in space, 2 s in time, and 1 km s^{-1} in Doppler velocity. A unique advantage of *IRIS* is the combination of spectra and slit-jaw images (SJIs), which provides simultaneous Doppler and POS velocity measurement and can thus constrain the true three-dimensional (3D) geometry and velocity vector. Its ultraviolet (UV) spectra cover a wide temperature range of 5×10^3–10^7 K and are particularly sensitive to chromospheric and transition-region temperatures of prominence material. With its $175'' \times 175''$ FOV covering the low corona, *IRIS* can provide critical clues to the initiation and early development of a CME/prominence eruption and complement instruments covering the high corona (e.g., coronagraphs and UVCS, which was turned off on 2012 December 15).

We report in this paper the first result of *IRIS* observations of an erupting prominence within a CME. We present the overview of observations in Section 2, data analysis results in Section 3, and concluding remarks in Section 4.

2. OVERVIEW OF OBSERVATIONS

On 2014 May 9, a major eruption involving a flare and a CME with a prominence eruption occurred in NOAA active region (AR) 12051 on the far side of the Sun. The flare kernel, observed by the Extreme UltraViolet Imager (EUVI) on the *Solar TErrestrial RElations Observatory* Ahead spacecraft (*STEREO*-A), was located 31° behind the west limb seen from the Earth perspective. Its POS projection, shown as the plus sign in Figure 1(a), was located at $(815'', -204'')$, 110″ inside the limb. The pre-event background removed full-disk EUVI 195 Å flux (Figure 1(d), blue line, at a 5-minute cadence) peaked at 02:21 UT and 1.16×10^7 photons s^{-1}, which translates to an equivalent *GOES* X-ray flare class of X1.6, according to empirical scaling (Nitta et al. 2013). The CME observed by *SOHO*/LASCO had a maximum POS speed of 1300 km s^{-1}, according to the CACTUS catalog (http://sidc.oma.be/cactus).

As seen by the Atmospheric Imaging Assembly (AIA) on the *Solar Dynamics Observatory* (*SDO*) in the He II 304 Å channel, the prominence eruption occurred in two episodes starting at 02:20 and 02:28 UT, with leading-edge speeds of 1060 and 1180 km s^{-1}, respectively. Episode 1 involved a single helical material thread expanding radially (Figure 1(a)). Episode 2 was more complex, consisting of sub-structured material bundles spanning a cone shape up to ~90° in angular extent (Figures 1(b) and (c)), whose central axis (along "Cut 1") was oriented 10° counterclockwise from the radial direction. Episode 2 lasted more than an hour up to 03:45 UT, with material being episodically ejected in some directions and at the same time falling back to the Sun in some other directions.

IRIS was running large coarse eight-step rasters with a step size of 2″ and 9.6 s cadence (8 s exposure) through 03:21 UT. SJIs in a single C II 1330 Å channel (bandwidth: 55 Å) covered a maximum $133'' \times 129''$ FOV, as shown in Figure 1(c). The *IRIS* slit, oriented at 13° clockwise from the eruption axis, missed the first episode but fully covered the second, which will be the focus of this paper. Table 1 summarizes the milestones of this event and corresponding coverage by different instruments.

3. *IRIS* DATA ANALYSIS

3.1. Wavelength Calibration

We performed on *IRIS* level-2 data *relative* (not *absolute*) wavelength calibration, which practically served our purpose of measuring the Doppler velocity of the eruption. Shown as the vertical dotted line in Figure 2, the reference wavelength for the Doppler velocity in each spectral line window was selected at the centroid of the corresponding line profile averaged over the on-disk portion of the slit through this event (02:17–03:21 UT). Therefore, all the Doppler velocities are measured with respect to the quiet-Sun region near the limb within the *IRIS* slit, which is located in the neighborhood of the eruption source region (the plus sign in Figure 1(a)).

The absolute uncertainty of this relative wavelength calibration can be estimated as follows. Taking the Mg II k λ 2796 line as an example, the sources of uncertainty include (i) the 20 mÅ wavelength shift (equivalent to 2 km s^{-1}) of this line measured near the solar limb from that at the disk center (Kohl & Parkinson 1976) and (ii) the *IRIS* orbital thermal variation of ~3 km s^{-1} (De Pontieu et al. 2014). These errors combined give an overall uncertainty of ~4 km s^{-1} for the absolute Doppler velocity, two orders of magnitude smaller than the typical values of hundreds of km s^{-1} measured in this eruption.

3.2. Temperature Distribution

The eruption was observed in C II 1330 Å SJIs and spectra of cool lines at chromospheric to transition region temperatures, including Mg II ($T \sim 10^4$ K), C II ($10^{4.3}$ K), Si IV ($10^{4.8}$ K), and O IV ($10^{5.2}$ K), as shown in Figure 2, corresponding to the erupting prominence material. *IRIS* detected no eruption-associated signal in the Fe XII 1349 Å ($10^{6.2}$ K) or Fe XXI 1354 Å ($10^{7.0}$ K) line, although AIA detected in its Fe XII 193 Å and Fe XIV 211 Å (~$10^{6.3}$ K) channels a dome-shaped, CME-generated EUV wave (e.g., Liu & Ofman 2014) appearing above the limb at 02:18 UT preceding the prominence eruption. We found no obvious delay among line intensities at different temperatures at a given spatial location and Doppler velocity, indicating no detectable temperature change of the erupting material passing through the *IRIS* slit.

3.3. Velocity Distribution: POS and Doppler

We selected a 20″ wide Cut 1 along the eruption axis to cover a large portion of the $14'' \times 129''$ region scanned by the *IRIS* slit and to obtain an AIA 304 Å space–time plot shown in Figure 1(e). The mass ejections exhibit ballistic-shaped trajectories, which were fitted with parabolic functions shown as dotted lines. We found a cascade of the ejections toward lower velocities at later times. As shown in Figure 1(f), the velocity at the top of the *IRIS* FOV (labeled s_1 in panel (e)) starts with 1180 ± 120 km s^{-1} at 02:29:01 UT and rapidly decreases to 430 ± 40 km s^{-1} at 02:30:30 UT, followed by a gradual drop to 66 ± 6 km s^{-1} at 02:44:24 UT. Ejections with speeds $\lesssim$200 km s^{-1} at s_1 turn back and start falling around 02:50 UT. In general, faster ejections reach greater heights and return to the *IRIS* FOV later at higher speeds. Figure 1(h) shows an *IRIS* C II 1330 Å SJI space–time plot from the same Cut 1 at higher resolution with similar behaviors because of its similar sensitivity (as He II 304 Å) to the ejected prominence material at typically transition-region/chromospheric

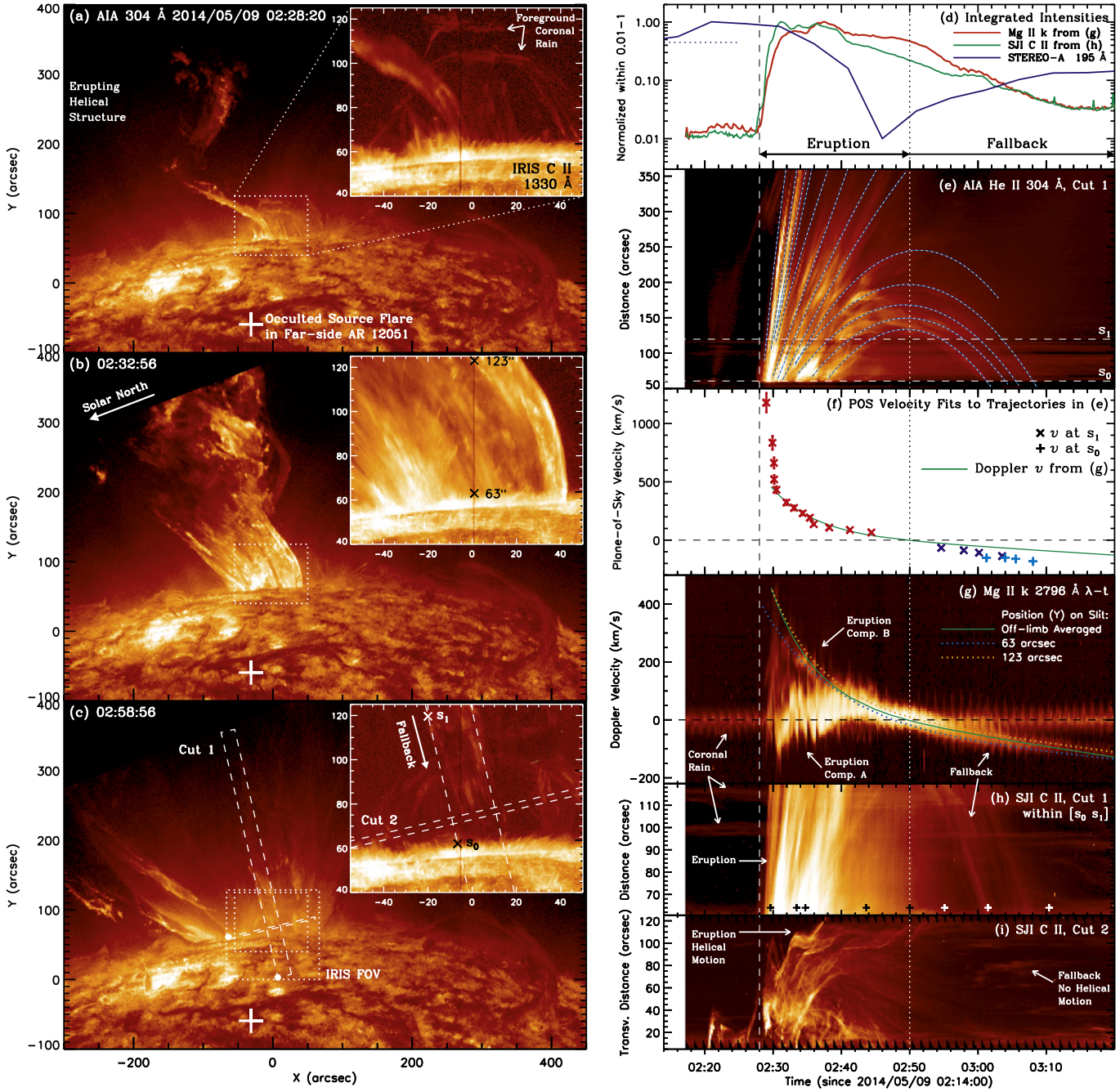

Figure 1. Images showing milestones of the CME/prominence eruption (left) and history of various quantities (right). (a)–(c) *SDO*/AIA 304 Å images rotated and shifted to match the *IRIS* orientation, with the origin of (*X*, *Y*) located at the center of the bottom edge of the *IRIS* FOV. (The accompanying online Animation 1 is oriented with solar west up.) The insets show simultaneous *IRIS* C II 1330 Å SJIs of the region within the small white box. The larger box in (c) indicates the original *IRIS* FOV. The two narrow rectangles are cuts used to obtain space–time plots in (e), (h), and (i), with the white filled circle denoting the start of the cut. The large plus sign shows the location of the source flare centroid detected by *STEREO*-A behind the limb. (d) Various light curves: *IRIS* Mg II k 2796 Å (red) and C II 1330 Å SJI (green) intensities obtained by vertically collapsing the corresponding space–time plots in (g) and (h), respectively, and *STEREO*-A EUVI 195 Å full-Sun flux (blue) with the pre-event background (blue dotted line) subtracted. (e) AIA 304 Å space–time plot obtained from Cut 1 (along the central axis of the ejection) shown in (c), overlaid with parabolic fits to trajectories shown in dotted lines. s_0 and s_1 here and in (c) mark the off-limb spatial range of the cut within the *IRIS* FOV. The velocities of the fitted trajectories at these two positions are shown in (f). (g) Mg II k λ–time plot by averaging spectra over all off-limb positions of the slit. The green curve here (and reproduced in (f)) is a parametric fit to the temporal transition from red- to blueshifts. Its counterparts in dotted lines are obtained from two off-limb positions (as marked in (b)), showing similar temporal evolution and indicating larger redshifts or smaller blueshifts at greater heights at any given time (as also shown in Figure 3(h)). (h and i) *IRIS* C II 1330 Å SJI space–time plots obtained from Cuts 1 and 2. The latter shows sinusoidal transverse displacements, manifesting unwinding motions of helical threads. The plus signs in (h) mark the times for the Mg II k/h ratio analysis shown in the bottom panels of Figure 4.

(An animation of this figure is available.)

temperatures (see Avrett et al. 2013 for more information on the C II 1330 Å formation temperature).

In the Doppler velocity distribution observed by *IRIS*, a striking feature is a *two-component composition* during the early phase of the eruption: a primary (A) bright and broad component being slightly blueshifted and/or mildly redshifted, and a secondary (B) highly redshifted, comparably faint and narrow component, as shown in Figure 2. The two components,

Table 1
Event Milestones on 2014 May 09

02:16/02:21	Flare onset/peak seen by *STEREO*-A (5-minute cadence)
02:18	EUV wave onset seen by *SDO*/AIA
02:20–02:28	Prominence eruption Episode 1 seen by *SDO*/AIA
	Max. POS speed 1060 km s^{-1} at ~02:21
02:28–03:45	Prominence eruption Episode 2 seen by *SDO*/AIA
	Max. POS speed 1180 km s^{-1} at ~02:29
02:28–03:21	*IRIS* slit coverage of Episode 2 eruption
	Max. redshift 460 km s^{-1} at 02:31
02:48	CME seen by *SOHO*/LASCO (24-minute cadence)
02:50	Transition from eruption to fallback within *IRIS* slit

yet with different structures, are somewhat parallel to each other, separated by ~200 km s^{-1}, with a similar trend of growing redshifts (up to 460 km s^{-1}) with height. They can be identified in all bright lines, including the Mg II k 2796 Å and h 2803 Å, C II 1335 and 1336 Å, and Si IV 1403 Å lines. (Note that the C II 1335 Å component B almost overlaps with the 1336 Å component A.) One possibility consistent with the gap between the two components is that the erupting material is spatially distributed in a *hollow*, rather than *solid*, cone shape.

As time progresses, the two components gradually merge into a single component with decreasing line widths. At later times, the entire spectrum evolves from red- to blueshifts, while maintaining the same general slope with height as noted below (see Figure 3, bottom). This evolution can be clearly seen from the wavelength– or velocity–time plot shown in Figure 1(g), obtained by averaging the Mg II k 2796 Å spectra over the entire region above the chromospheric limb. We fitted the velocity–time positions of component B and later the merged single component with a smooth spline function, shown as the solid green curve, to characterize the temporal evolution. This curve exhibits an initially rapid and then gradual decline with time, similar to that of the POS velocity shown in Figure 1(f). More interestingly, its crossing at zero Doppler velocity, i.e., the change from red- to blueshifts at 02:50 UT (marked by the vertical dotted line), *coincides with* the switch of sign for the POS velocity and the apexes of the ballistic POS trajectories shown in Figure 1(e), indicating a transition from upward eruption to downward fallback of the material. This transition may also explain the onset of the faster drop of the Mg II k 2796 Å intensity at the same time (see Figure 1(d), red line). The uncertainty of this temporal coincidence is estimated at ±2 minutes, bracketed by the zero-crossings of the two dotted lines in Figure 1(g), which are the counterparts of the solid curve obtained near the bottom and top edges of the off-limb portion of the *IRIS* slit (at $Y = 63''$ and $123''$; see Figure 1(b)). This conservative error estimate can also account for the temporal spread of the turning points of the different POS trajectories shown in Figure 1(e) and the ~4 km s^{-1} uncertainty in the absolute Doppler velocity noted in Section 3.1.

We also note in Figure 1(g) a persistent feature near zero Doppler shift, which is coronal rain in the foreground of the eruption. Because it is captured by the slit near the apexes of coronal loops where such cooling condensation is initially formed (e.g., Antolin et al. 2010; Liu et al. 2012; Fang et al. 2013), its small Doppler velocity, almost symmetrically distributed around zero, is expected and consistent with our selection of the reference wavelength described in Section 3.1.

We can estimate the 3D velocity vector using simultaneous POS and Doppler velocities. For example, during 02:30–02:45 UT, the two velocities (Figure 1(f), red crosses and green curve) are almost the same, indicating an angle of ~45° behind the POS. This is an upper limit, because the eruption component B has the highest redshift. A more accurate estimate can be obtained during the late phase when the velocity distribution is relatively simple. At 03:06:15 UT (see Figure 3(h)), for instance, the fallback material exhibits blueshifts increasing almost linearly with decreasing heights. This is consistent with a similar trend of the POS velocity (white dashed line) obtained from the last parabolic trajectory in Figure 1(e) covering this time. Specifically, the blueshift increases from −72 km s^{-1} to −98 km s^{-1} by 36% over the POS height range of 43 Mm ($59''$) within the *IRIS* FOV. This percentage change is similar to the 33% increase of the POS velocity from −137 km s^{-1} at 03:03:32 UT to −182 km s^{-1} at 03:08:04 UT over the same height range. These two pairs of velocities give a consistent angle of $(72/137) \approx (98/182) = 28°$ between the velocity vector and POS. This provides additional support for our interpretation of the late-phase blueshift as evidence of material falling back, and it implies that the fallback trajectory within this height range is oriented at a constant angle from the POS.

This parabolic space–time trajectory yields a downward POS acceleration of 165 m s^{-2} = 0.60 $g_\odot$, which translates to a true 3D acceleration of $0.60\, g_\odot/\cos(28°) = 0.68\, g_\odot$, where $g_\odot = 274$ m s^{-2} is the solar surface gravitational constant. Note that Cut 1 (along which this trajectory is measured) is only 10° from the POS projection of the radial direction and the 28° angle of the velocity vector from the POS is close to the 31° angle of the behind-the-limb location of the source flare. Therefore, this fallback path is likely close to the local vertical at the source[9] and the effective gravitational acceleration along it is close to $g_\odot$, greater than the measured 0.68 $g_\odot$. Such a less-than-free-fall acceleration, indicating cancellation of gravity by some upward force, is comparable to those (mostly measured in POS) of fallback material in chromospheric jets (e.g., Liu et al. 2009) and of coronal rain (e.g., Schrijver 2001; Antolin & Rouppe van der Voort 2012), but somewhat higher than those of downflow threads in quiescent prominences (e.g., Chae 2010; van Ballegooijen & Cranmer 2010; Liu et al. 2012; Low et al. 2012).

Another interesting feature of the fallback material is its narrow line width, which continues decreasing with time, as shown in Figure 1(g). During the late phase after 03:10 UT (e.g., Figures 3(h) and 4(c)), its 1/e nonthermal line width is only on the order of 10 km s^{-1}, nearly 50% that of the foreground coronal rain at loop apexes. This indicates that such material falls along streamline trajectories with very little velocity scatter or nonthermal broadening. We speculate that this could be due to the lack of line broadening agents, such as small-scale Alfvén waves or turbulence, which likely accompany the impulsive eruption earlier but have diminished substantially ever since.

[9] The exact 3D path of the fallback material is difficult to infer in this case, because of the inadequate cadence of *STEREO*-A and thus the unknown landing site behind the limb.

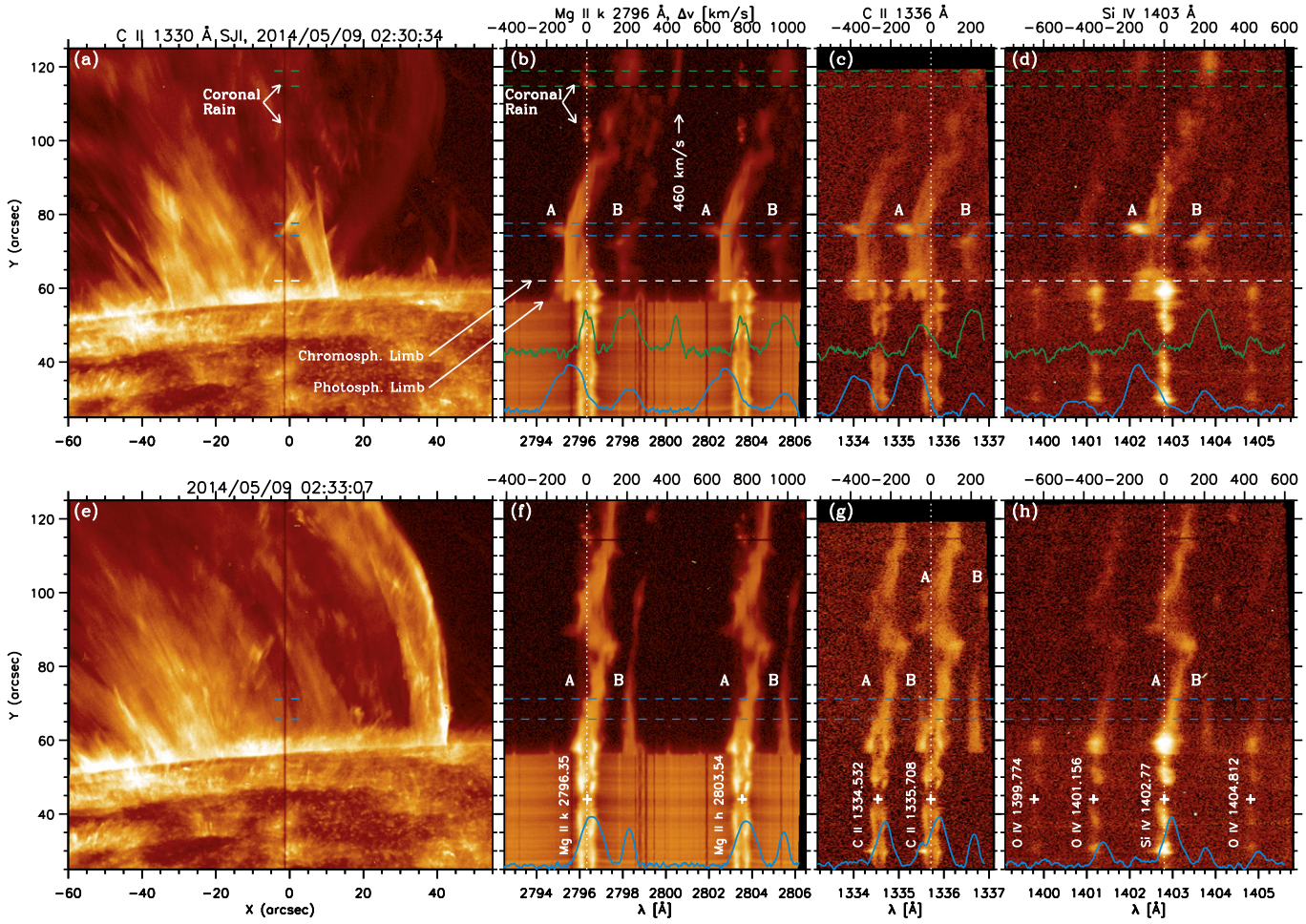

Figure 2. C II 1330 Å SJI (left) and simultaneous spectra in three line windows (right; see Animation 2), Mg II k 2796 Å, C II 1336 Å, and Si IV 1403 Å, for two selected times (top and bottom). The highest Doppler shift in the eruption of 460 km s^{-1} is identified in (b). In each spectral panel, the top *x*-axis shows the Doppler velocity, whose reference wavelength (see text in Section 3.1) is marked by the vertical dotted line. The plus signs in the bottom panels denote the nominal rest wavelengths of bright lines. Each pair of horizontal dashed lines defines the height range for the spectrum to be averaged to obtain the logarithmic profile shown at the bottom in the corresponding color. The horizontal white dashed line in the top panels indicates the height of the chromospheric limb (transition region) at the slit position shown on the left. "A" and "B" label the two components (primary and secondary) of the eruption in velocity space.

(An animation of this figure is available.)

3.4. Helical Structure and Torsional Motions

Helical structures have been commonly seen in imaging or spectroscopic observations of solar eruptions, including CMEs (e.g., Kohl et al. 2006), prominence eruptions (Koleva et al. 2012), and jets or surges (Canfield et al. 1996; Liu et al. 2011). We found compelling new evidence in this event, with the combination of high-resolution SJIs and spectra offering critical clues to the 3D structure.

In the POS, AIA images show corkscrew-shaped threads, especially early in the eruption when the morphology is relatively simple (e.g., Figures 1(a) and (b)). Their temporal evolution is manifested in the multiple sinusoidal tracks shown in Figure 1(i), an *IRIS* C II 1330 Å SJI space–time plot obtained from Cut 2, perpendicular to the eruption axis. In contrast, during the late phase, e.g., after 03:00 UT, the falling material shows no longer sinusoidal, but essentially flat tracks. This suggests that the pre-stored magnetic helicity or twists have been transported into the heliosphere by the eruption, and thus the falling material returns as streamline flows along untwisted field lines, similar to those in previously reported helical jets (e.g., Liu et al. 2009).

Doppler measurements by *IRIS* provide several clues for the interpretation of the above POS observations as torsional/rotational motions, rather than transverse oscillations. The *IRIS* slit is oriented at 13° clockwise from the central axis of the eruption, allowing it to cover both sides of the axis, i.e., with its lower portion sampling the left-hand side and the upper portion sampling the right-hand side. We find that early in the eruption, the initial blueshifts of some individual features switch to redshifts *with time* as they travel upward along the slit (see Figures 3(a)–(c) and Animation 2 for an example). Moreover, in *single spectral snapshots*, the primary (A) spectral component of the eruption at times shows predominant blueshifts at lower heights that smoothly transition to redshifts at larger heights (e.g., Figures 2(b) and 3(c)). The combination of these observations indicates a *counterclockwise rotation* of the erupting material when viewed top-down. Note that sometimes both components A and B show no sign of blueshifts but only redshifts that generally grow with height. This can be explained by the fact that the eruption occurs behind the limb and large redshifts due to outward radial motions are expected and can reduce or even reverse the blueshifts caused by rotations.

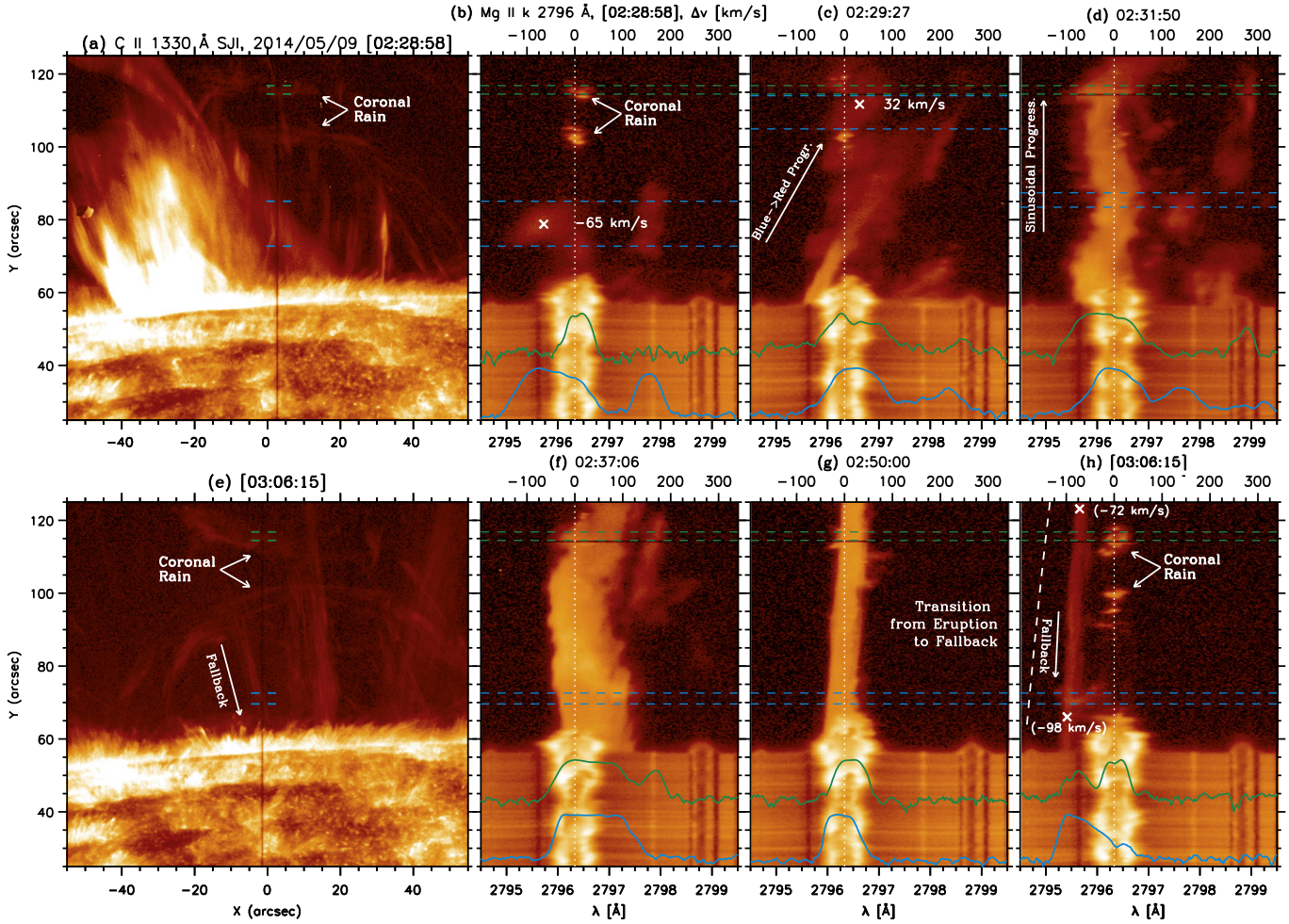

Figure 3. Same as Figure 2 but for the Mg II k 2796 Å line alone at six selected times showing the detailed spectral evolution (see Animation 3). The corresponding times between the SJIs and spectra are shown in brackets. (b) and (c) show the blue- to redshift progression (e.g., from −65 to 32 km s^{-1}) with time and height of a single feature, while (d) shows an upward sinusoidal progression across the entire slit, both indicative of helical motions during the eruption. (f) and (g) show the two eruption components (A and B; see Figure 2) gradually merging into one, which then decreases in line width with time and evolves from red- to blueshifts, while maintaining its generally constant slope with height. (h) Blueshifted spectrum of the falling material with narrow line widths during the late phase. The cross signs mark its line centroids at the top and bottom of the off-limb region. The white dashed line is the POS velocity as a function of distance (*y*-axis) from the last parabolic fit shown in Figure 1(e), which covers this time and the *IRIS* FOV. Like the blueshifts, it exhibits a similar growth with decreasing heights, indicating a true 3D downward acceleration of the falling material.

(An animation of this figure is available.)

We can further infer the handedness of the helices by combining POS and Doppler observations. Early in the event, SJIs show material threads progressing transversely from left to right. To be consistent with the above- inferred counterclockwise rotations with dominant blueshifts on the left, such threads must be located on the *front side* of the eruption, although the C II 1330 Å SJI emission is likely optically thin above the C II limb, and thus we are seeing both the front and back sides. Noting that these threads are oriented from lower right to upper left, we conclude that they are *left-handed helices*. Their counterclockwise rotations are thus consistent with relaxation or unwinding, rather than tightening, motions of the helices, which are expected for such an eruption.

We also found sinusoidal spectral variations along the slit and their progression toward greater heights with time, best seen during 02:31:12–02:32:19 UT (Figure 3(d)). This may be evidence of (multiple) small-scale (~10 Mm across) helical sub-structures within the overall eruption, which are also evident in SJIs (e.g., see the unfolding feature near 02:45 UT in Animation 2).

3.5. Mg II k/h Line Ratio and Doppler Dimming

3.5.1. Mg II k/h Line Ratio

The Mg II k 2796 Å and h 2803 Å lines and their intensity ratio can provide useful plasma diagnostics (e.g., Leenaarts et al. 2013; Pereira et al. 2013). In general, this k/h ratio is expected to be ~2 for optically thin, collisionally excited (thermal) emission. Previously reported values include 2 for an AR prominence (Vial et al. 1979), 1.7 for a quiescent prominence (Vial 1982a), and 1.33–1.35 for quiescent prominences recently observed by *IRIS* (Heinzel et al. 2014; Schmieder et al. 2014).

As shown in Figure 4 (top), we identified various corresponding features in both the k and h lines, integrated their continuum-subtracted intensities, and obtained their ratios, which are labeled together with the line-centroid Doppler

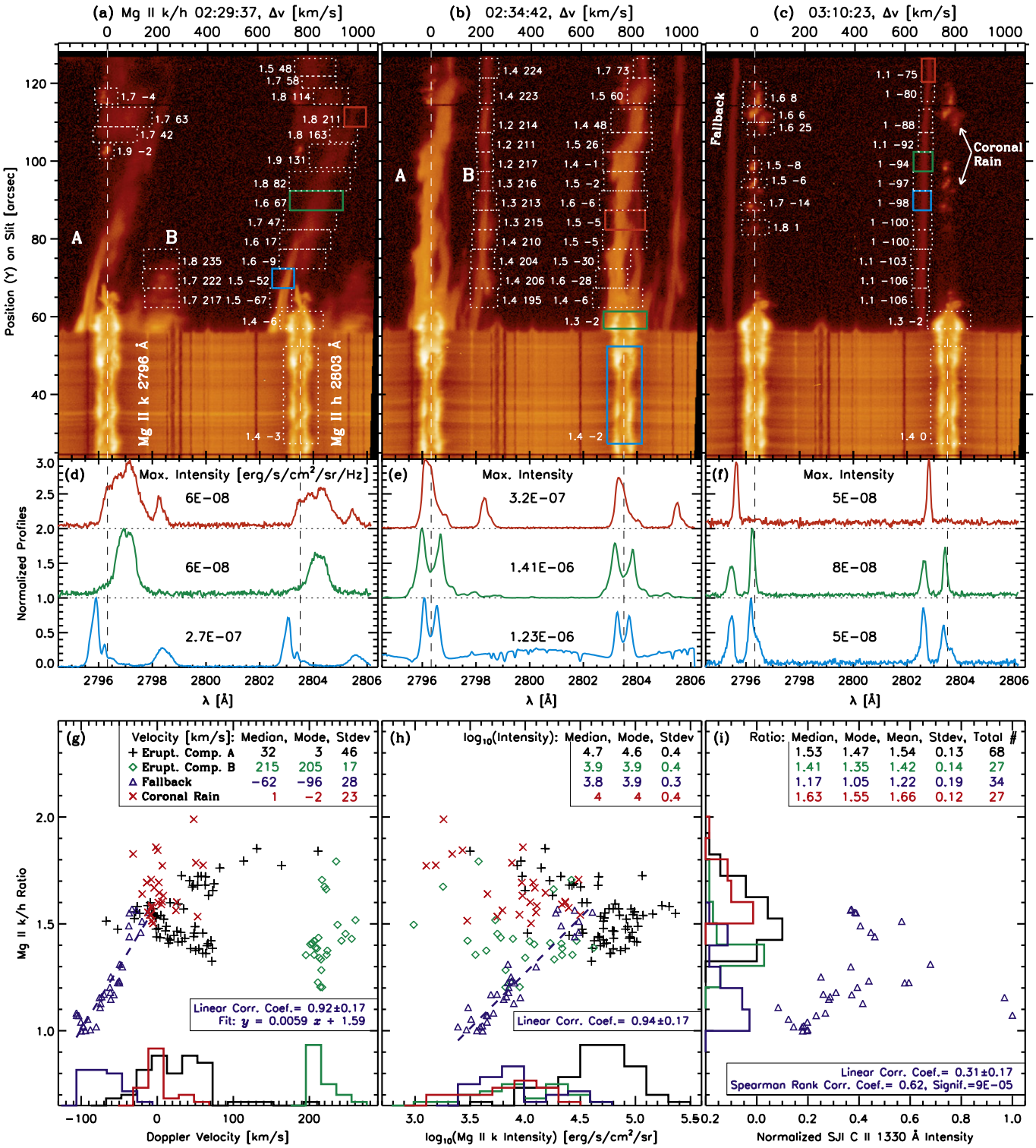

Figure 4. Analysis of the Mg II k 2796 Å to h 2803 Å integrated line intensity ratio. (a)–(c) Mg II k and h spectra at three selected times, showing the primary (A) and secondary (B) eruption components in (a) and (b) and the fallback material together with the foreground coronal rain in (c). The boxes mark individual features selected for line ratio analysis, each labeled with the corresponding ratio and line-centroid Doppler velocity (in km s^{-1}). The vertical dashed lines indicate the rest wavelengths. (d–f) Spectra averaged over the height ranges of selected boxes in corresponding colors shown above. Each profile is normalized and vertically shifted by multiples of unity. The number indicates the maximum of each profile in units of erg s^{-1} cm^{-2} sr^{-1} Hz^{-1}. (g) k/h intensity ratio vs. line-centroid Doppler velocity from eight different times (including those of (a)–(c)) during the course of the event, as marked by the plus signs in Figure 1(h), at the same raster position. The results are color-coded for four different features: the primary (A; black plus signs) and secondary (B; green diamonds) eruption components, fallback material (blue triangles), and coronal rain (red crosses). Their Doppler velocity histograms are plotted at the bottom, with the median, mode, and standard deviation values shown on the top. The fallback material exhibits a linear correlation between the two quantities, to which a linear fit is shown as the dashed line. (h) Same as (g) but for the logarithmic k line intensity as the *x*-axis. (i) Histograms of the k/h intensity ratios of the four features plotted against the *y*-axis. The fallback material k/h ratio is also plotted vs. the normalized SJI C II 1330 Å intensity on the *x*-axis, showing a comparably weak but noticeable correlation.

velocities. The middle row in Figure 4 shows some sample spectra at selected positions. Unlike their on-disk or chromospheric counterparts, the off-limb Mg II k and h lines of both erupted material and coronal rain have no central reversal, similar to those in *IRIS* observed prominences (Heinzel et al. 2014; Schmieder et al. 2014), suggestive of a low pressure or thickness and optically thin regime. Because the oscillator strength of the k line is twice that of the h line, the k line always has a larger integrated intensity. However, for the fallback material (Figure 4(f)), the k line has a comparably lower peak intensity.

We repeated this analysis for a total of 156 features selected from eight spectra through the course of this event. The resulting intensity ratio is plotted against the line-centroid Doppler velocity and k line intensity (Figures 4(g) and (h)), categorized for four types of features: the primary (A; black plus signs) and secondary (B; green diamonds) eruption components, fallback material (blue triangles), and coronal rain (red crosses). As a reference, the k/h ratios of the on-disk quiet Sun and chromosphere at the limb have medians and standard deviations of 1.38 ± 0.02 and 1.34 ± 0.02, respectively. The coronal rain has the highest k/h ratio of 1.63 ± 0.12, the lowest Doppler velocity nearly zero, and a moderate intensity. Eruption component A has a moderate k/h ratio of 1.53 ± 0.13, a small Doppler velocity, and the highest intensity of $10^{4.7}$ erg s^{-1} cm^{-2} sr^{-1}. Eruption component B has a somewhat smaller ratio of 1.41 ± 0.14, the highest Doppler velocity of >200 km s^{-1} redshifts, and a moderate intensity about 6 times smaller than that of component A. The fallback material has the lowest k/h ratio of 1.17 ± 0.19, a moderate blueshift, and the lowest intensity.

The k/h ratios of the fallback material are particularly interesting, yet puzzling. During the late phase of the event, as progressively less material is present off-limb and as the intensity drops with time, one would expect the Mg II k and h emission to approach the optically thin regime and thus a k/h ratio close to 2. However, the 1.17 median ratio is surprisingly small, the lowest among all reported values for prominences and even less than those of the quiet-Sun disk (1.38 ± 0.02) and chromosphere (1.34 ± 0.02). More interestingly, the k/h ratio $R_{\rm k/h}$ is highly correlated with both the line-centroid Doppler velocity $v_{\rm D}$ and the k line intensity $I_{\rm k}$, with linear correlation coefficients of 0.92 ± 0.17 and 0.94 ± 0.17, respectively. A linear regression gives $R_{\rm k/h} = 0.0059 v_{\rm D}/(100$ km s^{-1}) + 1.59, leading to a ratio of unity at $v_{\rm D} = -100$ km s^{-1}.

We also obtained C II 1330 Å SJI intensities averaged within the *Y*-direction ranges corresponding to those boxes defined in the spectra of the fallback material (e.g., Figure 4(c)) and within an *X*-direction range of 14″ covering all the eight-step raster positions. They show a comparably weak but noticeable correlation with the k/h ratios. This is perhaps not surprising because of the similar temporal trends of the C II 1330 Å SJI and Mg II k line intensities, as shown in Figure 1(d).

3.5.2. Doppler Dimming

Compared with the eruption components A and B with a complex morphology and dynamic evolution but lack of correlation in Figures 4(g) and (h), the fallback material has a relatively simple morphology in a relaxed, post-eruption state and a well-defined correlation between the Mg II k/h ratio and the Doppler velocity or line intensity. In this section, we thus focus on the fallback material to explore the underlying physics of such characteristics as the surprisingly low values of the k/h ratio. We note that the off-limb k and h lines have contributions from both radiative excitation by the solar surface radiation and local collisional (thermal) excitation. Their relative importance depends on the pressure (density and temperature) of the material and is estimated as follows.

We assume that the Mg II line emitting plasma is optically thin, an assumption valid only for thin, low-pressure prominence threads (see Table 2 of Heinzel et al. 2014). Then each plasma blob receives the full incident radiation and emits both scattered ($I_{\rm sc}$) and thermal ($I_{\rm th}$) radiation. Regardless of the frequency redistribution process, $I_{\rm sc}$ is the product of the geometric dilution factor and the chromospheric intensity, for which we adopt the line-center intensity of 3×10^{-7}erg s^{-1} cm^{-2} sr^{-1} Hz^{-1} from Heinzel et al. (2014). $I_{\rm th}$ is the product of the photon destruction probability ε and the Planck function B_ν at the plasma temperature T (see, e.g., Mihalas 1978 p. 650; Vial 1982b). ε is proportional to the electron density $n_{\rm e}$ and steadily increases with T (so does B_ν). We find that

1. for a typical prominence density of $n_{\rm e} \sim 10^{11}$ cm^{-3} (e.g., see Table 4 of Labrosse et al. 2010) and a low temperature of $T = 6 \times 10^3$ K, the radiation term $I_{\rm sc}$ dominates over the collisional term $I_{\rm th}$ by orders of magnitude, while
2. an increase in density above 10^{12} cm^{-3} and/or in temperature to 1.5×10^4 K would result in the collisional-term dominance.

Determining the relative importance of $I_{\rm sc}$ and $I_{\rm th}$ for the specific event under study requires knowledge of the plasma density. To this end, we utilized the density-sensitive O IV 1399.774/1401.156 Å line ratio. In order to increase the signal-to-noise ratio, we first obtained a spectrum (see Figure 5(a)) by averaging two raster scans when these lines are relatively bright and overlaps due to Doppler shifts are relatively small. We then averaged all off-limb spectra to obtain the profile shown in Figure 5(b), which then gives a continuum-subtracted, integrated O IV 1399.774/1401.156 Å intensity ratio of 0.234 for the primary (A) eruption component. According to the CHIANTI v7.1 database (Landi et al. 2013), this ratio translates to a predicted density of $n_{\rm e} = 2.6 \times 10^{10}$ cm^{-3} (see Figure 5(c)). Its uncertainty originates mainly from line blending, which is estimated as follows: (i) We found that the O IV 1399.774 Å line is blended by the Fe II 1399.962 Å line at an upper-limit 6% level. To arrive at this order-of-magnitude estimate, we assumed that the Fe II and Mg II k lines are emitted by the same optically thin plasma of a uniform differential emission measure (not necessarily true). We used the CHIANTI routine `ch_synthetic.pro` and assumed a constant pressure (corresponding to $n_{\rm e} = 10^{11}$ cm^{-3} and $T = 10^4$ K for typical prominence conditions) to synthesize their respective contribution functions $G(T)$, which were then multiplied by the chromospheric abundance and the *IRIS* response function (from `iris_get_response.pro`) and integrated over a temperature range of 10^4–10^5 K covering the $G(T)$ peak to yield their line intensities, $I_{\rm Fe\ II}$ and $I_{\rm Mg\ II\ k}$. With the predicted ratio of $I_{\rm Fe\ II}/I_{\rm Mg\ II\ k} = 3.7 \times 10^{-4}$ and the observed Mg II k intensity, we estimated the Fe II 1399.962 Å intensity, which turned out to be $\leqslant 6\%$ of the observed O IV 1399.774 Å intensity. (ii) We

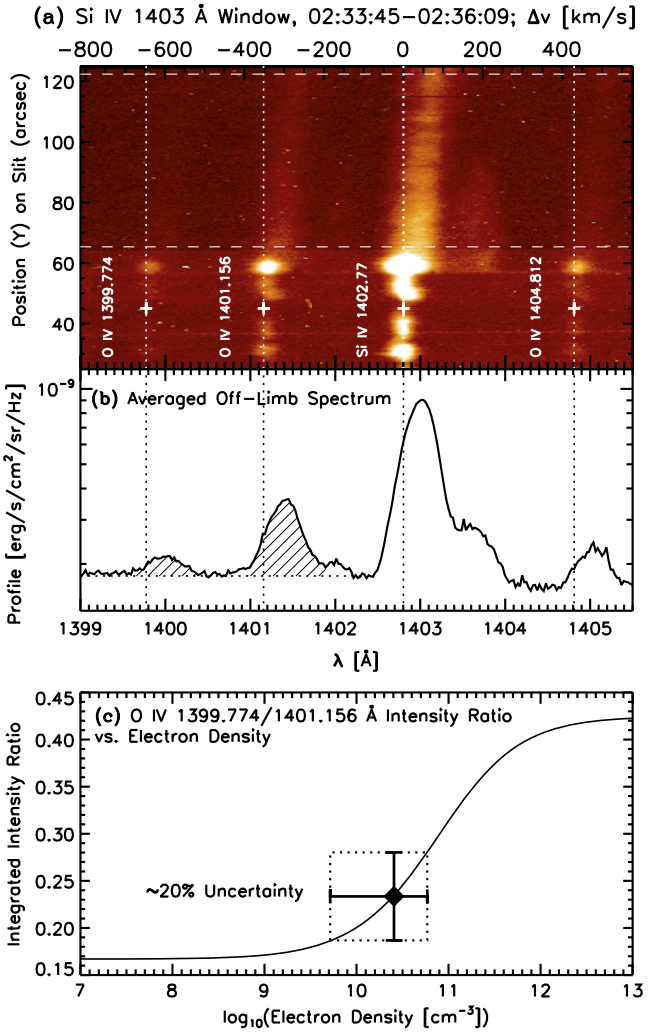

Figure 5. Density estimate using the O IV 1399.774/1401.156 Å line ratio. (a) Spectrum of the Si IV 1403 Å window averaged over 16 spectra of two raster scans during 02:33:45–02:36:09 UT. (b) Spectrum averaged over the off-limb region between the two horizontal dashed lines in (a). The O IV 1399.774 and 1401.156 Å line intensities of the primary eruption component (A) integrated over the two hatched areas give a ratio of 0.234, shown as the diamond in (c). The curve in (c) is the CHIANTI-predicted line ratio as a function of electron density.

could not identify any S I 1401.514 Å line emission beyond the quiet-Sun disk, and thus its blend to the O IV 1401.156 Å line is considered negligible. Nevertheless, we assumed a conservative 20% uncertainty for the line ratio, which gives a density range of 5.2×10^9 to 5.9×10^{10} cm^{-3}. This density pertains to the warm plasma at the O IV formation temperature of $\sim 10^{5.2}$ K, which, in this case, is most likely located in the so-called prominence–corona transition region (PCTR; Parenti & Vial 2014). In the cold prominence core at the Mg II k and h formation temperature of $\sim 10^4$ K, the density could be 10 times higher (assuming pressure equilibrium), but still smaller than the extreme density of $\geqslant 10^{12}$ cm^{-3} required for the collisional-term dominance in the low-temperature regime as mentioned above. Therefore, we conclude that the Mg II k and h emission of the erupted material is dominated by radiative excitation.

For radiatively excited emission from moving objects, there is a *Doppler dimming* effect in which the incident line emission from the solar surface is Doppler-shifted out of resonance. This effect has been extensively investigated for hydrogen and helium lines (e.g., Hyder & Lites 1970; Heinzel & Rompolt 1987; Gontikakis et al. 1997; Labrosse et al. 2007; Labrosse & McGlinchey 2012) and recently modeled for the Mg II k and h lines (Heinzel et al. 2014, 2015). Note that the wings of the chromospheric k and h lines are somewhat different. Therefore, when a moving object resonantly absorbs the Doppler-shifted wings followed by de-excitation radiation, the emergent k/h ratio can depend on the Doppler velocity. This may potentially explain their observed correlation.

As a proof-of-concept exercise, we model the Mg II k/h ratio due to Doppler dimming as follows. Again, we assume that the erupted material is optically thin and ignore collisional excitation according to the above analysis. Thus, the Mg II k and h emission is simply resonant scattering of the incident chromospheric radiation, with no radiative transfer taking place. We also assume that the solar surface is a sphere producing uniform radiation, for which we adopt an *IRIS*-observed quiet-Sun Mg II k and h spectrum, and ignore limb darkening or brightening. For an object at a height h moving at a velocity v_r in the radial direction, we calculate its incident radiation by integrating the Doppler-shifted radiation from the entire visible solar surface, as schematically shown in Figure 6(a). This spatial average can alter the shape of the absorbed line profile, because the radial velocity v_r has different parallel components $v_{\rm para}$ projected along incident rays from different directions that determine the Doppler shifts. As an example, Figures 6(b) and (c) show the average Mg II k and h profiles incident on an object moving at different velocities at a height of 100 Mm, which is near the lower limit of the height range of the *IRIS*-observed prominence material according to its behind-the-limb source location. At $\gtrsim 50$ km s^{-1}, the central reversals of both lines disappear. Because Mg is a heavy element, the thermal broadening is expected to be small and we assume a delta-function profile for the scattering agent (moving object). Thus, the scattered emission is essentially the incident radiation at the line center ($\Delta v = 0$), as marked by the vertical dashed line. The ratio of the k and h intensity at this position, as shown in Figure 6(d), would be equivalent to the observed line ratio. For a stationary object ($v_r = 0$), this k/h ratio is $R_{\rm k/h} = 1.20$. For a moving object, the two lines are dimmed by different factors. At $v_r = -100$ km s^{-1}, for example, the k line center intensity is reduced by a factor of 0.10, while the h line by 0.14, leading to $R_{\rm k/h} = 1.20 \times (0.10/0.14) = 0.87$. Such dimming factors are on the same order of magnitude as those modeled for a moving prominence (Heinzel et al. 2014).

Repeating this for different height h and velocity v_r values, we obtained the dependence of the k/h ratio $R_{\rm k/h}$ on these two quantities, as shown in Figure 6(e). These curves have a butterfly shape and generally decrease with increasing v_r or h. There is a positive correlation between $R_{\rm k/h}$ and v_r near $v_r = -100$ km s^{-1} (<0 for falling material), which qualitatively agrees with the observed correlation shown in Figure 4(g). A blue-red asymmetry is present, with smaller k/h ratios for radially outward velocities ($v_r > 0$), because of the asymmetry in the Mg II k and h wings. For lower heights, the butterfly curves have a broader top portion at values close to that at $v_r = 0$, because relatively more incident radiation originates from large angles away from the local radial direction at the object. Such radiation is less Doppler-shifted due to the smaller $v_{\rm para}$ component of the assumed radial velocity projected along those rays.

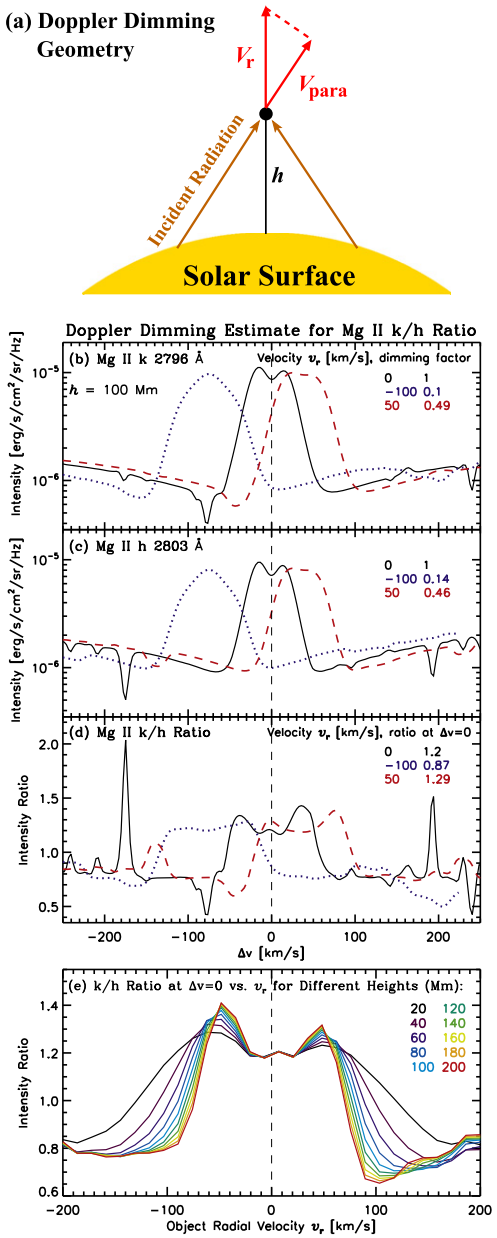

Figure 6. Empirical modeling of the Mg II k/h line ratio due to Doppler dimming. (a) Schematic geometry for Doppler dimming estimate. (b and c) Mg II k 2796 Å and h 2803 Å line profiles (centered at their respective rest wavelengths) averaged over the entire visible solar disk as seen by a radially moving object at three velocities ($v_r = -100$, 0, 50 km s^{-1}) and a fixed height $h = 100$ Mm, with their corresponding k/h ratios shown in (d). (e) Mg II k/h line ratio at the line center ($\Delta v = 0$), as shown in (d), as a function of the object's radial velocity v_r for a range of color-coded heights (20–200 Mm). A positive correlation is present for falling material ($v_r < 0$), in qualitative agreement with the correlation shown in Figure 4(g).

Note that the eruption component B is about 200 km s^{-1} higher in Doppler velocity and a factor of 6 fainter in intensity than component A, and even fainter than the coronal rain. We suggest that Doppler dimming may contribute to its faintness, among other possible factors, such as a smaller emission measure. We also note that the gradual fading of the C II 1330 Å SJI intensity during the late phase (see Figure 1(d) and online Animation 2) coincides with the increasing blue-shifts and POS downflow velocities. We speculate that this fading may be due, at least in part, to Doppler dimming of the C II lines in a similar manner. In contrast, Doppler dimming has very little effect on the coronal rain detected near the loop apexes because of its small velocities.

4. CONCLUDING REMARKS

4.1. Summary

We have presented the first *IRIS* observations of a fast prominence eruption associated with a CME and an equivalent X1.6 flare on the far side of the Sun. We summarize our major findings as follows.

1. The ejected material is detected in bright lines at chromospheric to transition-region temperatures (10^4–$10^{5.2}$ K). We find no obvious delay among lines at different temperatures, suggesting *no detectable temperature changes* (see Section 3.2).

2. The prominence eruption has a maximum POS velocity of ~1200 km s^{-1}and redshift of 460 km s^{-1}, while the white-light CME has a maximum POS speed of 1300 km s^{-1} (Section 3.3). These values are near the *higher end* of the velocity distribution reported for prominence eruptions. In contrast, the Doppler velocities of prominence material in the slower CME interior detected by *SOHO*/UVCS are on average only ~10% of the POS speeds of the CME leading fronts seen by *SOHO*/LASCO (Giordano et al. 2013).
3. The erupting material exhibits a cascade with time toward lower velocities, with a transition from upward ejection to downward fallback consistently manifested in *both POS velocities and Doppler shifts* (red to blue drift). During the fallback phase, at a given time, larger blueshifts are found at lower heights, consistent with the downward acceleration of the falling material; at a given height, the blueshift increases with time, consistent with the fact that material falling later returns from greater heights and is originally ejected at larger initial velocities earlier. A typical fallback trajectory has a less-than-free-fall, true 3D acceleration of 0.68 $g_{\odot}$, comparable to the values reported for falling ejecta and coronal rain. The fallback material exhibits a progressively narrower line width down to ~10 km s^{-1}, indicative of streamline flows (see Section 3.3).
4. There are *two components* of erupted material in Doppler velocity: a primary (A), bright component of comparably small Doppler shifts and a secondary (B), faint, highly redshifted component. The two components are separated by ~200 km s^{-1}, suggestive of a hollow, rather than solid, cone shape, in which the material is distributed (Section 3.3). We also suggest that stronger Doppler dimming of component B can contribute to its relatively smaller intensity.
5. The combination of a blue- to redshift transition with height along the slit and corkscrew-shaped threads and sinusoidal transverse motions imaged in the POS indicates that the eruption involves a *left-handed helical structure* undergoing counterclockwise (when viewed top-down) unwinding/relaxation motions (Section 3.4). Such a handedness originating from the southern hemisphere (AR 12051) is opposite to the dominant hemispheric rule of magnetic helicity for ARs (e.g., Pevtsov et al. 1995; Wang 2013).
6. We find a wide range of Mg II k/h line intensity ratios. The foreground coronal rain has the highest median ratio of 1.63, the eruption components A and B have intermediate values of 1.53 and 1.41, respectively, while the fallback material has the lowest value of 1.17, the *smallest ever reported*. In addition, the k/h ratio of the fallback material is *strongly correlated* with the Doppler velocity and line intensity, with linear correlation coefficients at $>5\sigma$ levels (Section 3.5.1).
7. The low density $n_e < 10^{12}$ cm^{-3} of the prominence core inferred from the O IV 1399.774/1401.156 Å line ratio implies that the observed Mg II k and h emission is dominated by radiative (rather than collisional) excitation. Doppler dimming is thus expected to alter the emergent emission profile from moving objects. Our simple back-of-envelope calculation demonstrates that this effect may qualitatively explain the observed Mg II k/h ratios, especially the surprisingly low values found in the fallback material and their correlation with Doppler velocities (Section 3.5.2).

4.2. Discussion

New *IRIS* observations, such as these presented here, have opened a new diagnostic window to study CMEs/prominence eruptions. For example, once the thermodynamic parameters establish that the Mg II k and h emission is dominated by resonance scattering, the k/h ratio can provide, through the Doppler dimming factor, critical information about the radial velocity, height, and 3D geometry of the ejected material. Similar techniques have already been used for diagnosing solar wind and CME speeds in the outer corona (e.g., Kohl & Withbroe 1982; Raymond & Ciaravella 2004).

Another interesting feature detected by *IRIS* is that the erupting and returning material behind the limb both appear at spicule heights within the chromosphere in all bright lines at large Doppler shifts (see Figure 2), alongside their corresponding rest-wavelength chromospheric emission at the foreground limb. These lines include the Mg II k and h and C II lines, which have central reversals in the chromospheric emission because of high opacity, but have no reversal in the Doppler-shifted, off-limb components, indicating a largely optically thin regime. In other words, IRIS *"sees through" the chromosphere at the limb* in certain Doppler-shifted lines of otherwise optically thick chromospheric emission. This is equivalent to detecting emission at different wavelengths from different LOS depths of the on-disk atmosphere. This capability of simultaneously detecting behind-the-chromospheric-limb, Doppler-shifted material and the foreground chromospheric material of the same temperature provides a useful diagnostic potential yet to be further explored, e.g., for partially occulted flares (e.g., Liu et al. 2008; Krucker & Lin 2008).

The proof-of-concept estimate of Doppler dimming presented in Section 3.5.2 has its limitations with assumptions that may not be valid in the real situation. It explains some, but not all, observed features, including some high Mg II k/h ratio (>1.6) of the highly redshifted eruption component B (Figure 4(g)). However, its promise demonstrated in the qualitative agreement with the observations warrants more detailed non-LTE modeling with the inclusion of, e.g., a 2D or 3D geometry, velocity vectors for Doppler dimming effects, and, as in Heinzel et al. (2014), the presence of a prominence–corona transition region, which we plan to pursue in the future. We also plan to use multi-instrument observations to infer the detailed 3D geometry and velocity vector, as well as the escaping and returning mass fluxes.

This work is supported by NASA contract NNG09FA40C (IRIS) and the Lockheed Martin Independent Research Program. W.L. thanks Paola Testa and Lucia Kleint for help with *IRIS* data analysis, *IRIS* planner Nicole Schanche for capturing this eruption, and Hui Tian and Adrian Daw for useful discussions.

REFERENCES

Antolin, P., & Rouppe van der Voort, L. 2012, ApJ, 745, 152
Antolin, P., Shibata, K., & Vissers, G. 2010, ApJ, 716, 154
Avrett, E., Landi, E., & McKillop, S. 2013, ApJ, 779, 155
Canfield, R. C., Reardon, K. P., Leka, K. D., et al. 1996, ApJ, 464, 1016

Chae, J. 2010, ApJ, 714, 618
Chen, P. F. 2011, LRSP, 8, 1
Ciaravella, A., Raymond, J. C., Fineschi, S., et al. 1997, ApJL, 491, L59
De Pontieu, B., Title, A. M., Lemen, J. R., et al. 2014, SoPh, 289, 2733
Fang, X., Xia, C., & Keppens, R. 2013, ApJL, 771, L29
Fontenla, J. M., & Poland, A. I. 1989, SoPh, 123, 143
Giordano, S., Ciaravella, A., Raymond, J. C., Ko, Y.-K., & Suleiman, R. 2013, JGRA, 118, 967
Gontikakis, C., Vial, J.-C., & Gouttebroze, P. 1997, A&A, 325, 803
Harra, L. K., Hara, H., Imada, S., et al. 2007, PASJ, 59, 801
Heinzel, P., & Rompolt, B. 1987, SoPh, 110, 171
Heinzel, P., Schmieder, B., Mein, N., & Gunár, S. 2015, ApJL, 800, L13
Heinzel, P., Vial, J.-C., & Anzer, U. 2014, A&A, 564, A132
Hundhausen, A. J., Sawyer, C. B., House, L., Illing, R. M. E., & Wagner, W. J. 1984, JGR, 89, 2639
Hyder, C. L., & Lites, B. W. 1970, SoPh, 14, 147
Jin, M., Ding, M. D., Chen, P. F., Fang, C., & Imada, S. 2009, ApJ, 702, 27
Kohl, J. L., Noci, G., Cranmer, S. R., & Raymond, J. C. 2006, A&ARv, 13, 31
Kohl, J. L., & Parkinson, W. H. 1976, ApJ, 205, 599
Kohl, J. L., & Withbroe, G. L. 1982, ApJ, 256, 263
Koleva, K., Madjarska, M. S., Duchlev, P., et al. 2012, A&A, 540, A127
Krucker, S., & Lin, R. P. 2008, ApJ, 673, 1181
Labrosse, N., Gouttebroze, P., & Vial, J.-C. 2007, A&A, 463, 1171
Labrosse, N., Heinzel, P., Vial, J.-C., et al. 2010, SSRv, 151, 243
Labrosse, N., & McGlinchey, K. 2012, A&A, 537, A100
Landi, E., Young, P. R., Dere, K. P., del Zanna, G., & Mason, H. E. 2013, ApJ, 763, 86
Leenaarts, J., Pereira, T. M. D., Carlsson, M., Uitenbroek, H., & de Pontieu, B. 2013, ApJ, 772, 89
Liu, W., Berger, T. E., & Low, B. C. 2012, ApJL, 745, L21
Liu, W., Berger, T. E., Title, A. M., & Tarbell, T. D. 2009, ApJL, 707, L37
Liu, W., Berger, T. E., Title, A. M., Tarbell, T. D., & Low, B. C. 2011, ApJ, 728, 103
Liu, W., & Ofman, L. 2014, SoPh, 289, 3233
Liu, W., Petrosian, V., Dennis, B. R., & Jiang, Y. W. 2008, ApJ, 676, 704
Low, B. C., Liu, W., Berger, T., & Casini, R. 2012, ApJ, 757, 21
Mackay, D. H., Karpen, J. T., Ballester, J. L., Schmieder, B., & Aulanier, G. 2010, SSRv, 151, 333
Martin, S. F. 1998, SoPh, 182, 107
Mihalas, D. 1978, Stellar Atmospheres (2nd ed.; San Francisco, CA: Freeman)
Nitta, N. V., Aschwanden, M. J., Boerner, P. F., et al. 2013, SoPh, 288, 241
Parenti, S. 2014, LRSP, 11, 1
Parenti, S., & Vial, J.-C. 2014, in IAU Symp. 300, Nature of Prominences and Their Role in Space Weather, ed. B. Schmieder, J.-M. Malherbe, & S. T. Wu (Cambridge: Cambridge Univ. Press), 69
Penn, M. J. 2000, SoPh, 197, 313
Pereira, T. M. D., Leenaarts, J., de Pontieu, B., Carlsson, M., & Uitenbroek, H. 2013, ApJ, 778, 143
Pevtsov, A. A., Canfield, R. C., & Metcalf, T. R. 1995, ApJL, 440, L109
Raymond, J. C., & Ciaravella, A. 2004, ApJL, 606, L159
Raymond, J. C., Ciaravella, A., Dobrzycka, D., et al. 2003, ApJ, 597, 1106
Schmahl, E., & Hildner, E. 1977, SoPh, 55, 473
Schmieder, B., Tian, H., Kucera, T., et al. 2014, A&A, 569, A85
Schrijver, C. J. 2001, SoPh, 198, 325
Schwenn, R. 1996, Ap&SS, 243, 187
st. Cyr, O. C., Plunkett, S. P., & Michels, D. J. 2000, JGR, 105, 18169
Tandberg-Hanssen, E. 1995, The Nature of Solar Prominences (Dordrecht: Kluwer)
Tian, H., McIntosh, S. W., Xia, L., He, J., & Wang, X. 2012, ApJ, 748, 106
Tian, H., Tomczyk, S., McIntosh, S. W., et al. 2013, SoPh, 288, 637
van Ballegooijen, A. A., & Cranmer, S. R. 2010, ApJ, 711, 164
Vial, J. C. 1982a, ApJ, 253, 330
Vial, J. C. 1982b, ApJ, 254, 780
Vial, J. C., Gouttebroze, P., Artzner, G., & Lemaire, P. 1979, SoPh, 61, 39
Wang, Y.-M. 2013, ApJL, 775, L46
Webb, D. F., & Howard, T. A. 2012, LRSP, 9, 3
Widing, K. G., Feldman, U., & Bhatia, A. K. 1986, ApJ, 308, 982
Wiik, J. E., Schmieder, B., Kucera, T., et al. 1997, SoPh, 175, 411